Promoting Polysulfide Redox Reactions and Improving Electronic Conductivity in Lithium-Sulfur Batteries via Hierarchical Cathode Materials of Graphene-wrapped Porous TiO_2 Microspheres with Exposed (001) Facets

Chenyang Zha,[a, ‡, *] Fengli Yang, [b, ‡] JunJie Zhang, [d, ‡] Tikai Zhang,[a] Shuai Dong,[d] Houyang Chen[c, *]

[a] Institute of Functional Nano and Soft Materials (FUNSOM), Jiangsu Key Laboratory for Carbon-Based Functional Materials and Devices, Soochow University, Suzhou, Jiangsu 215123, China.

[b] School of Chemistry and Environmental Engineering, Jiangsu University of Technology, Changzhou, 213001, China.

[c] Department of Chemical and Biological Engineering, State University of New York at Buffalo, Buffalo, New York 14260-4200, USA.

[d] School of Physics, Southeast University, Nanjing, Jiangsu 211189, China.

‡ These authors contributed equally to this work.

* Corresponding authors.
E-mail: zha@suda.edu.cn
E-mail: hchen23@buffalo.edu

Contents

Section S1. Experimental sections

Section S1.1 Preparation of GN-wrapped nanoporous anatase microspheres with exposed (001) facets

Nanoporous TiO_2 microspheres were synthesized through a facile hydrothermal reaction. In a typical synthesis, 0.5 g ammonium bi-fluoride was first added in 50 mL 30 wt% hydrogen peroxide, which was stirred for 10-50 minutes. Then, 1-2 ml titanium tetrachloride was added, and the solution was stirred for another 30-60 min. 15 ml of the above solution was transferred into a 30 mL Teflon-lined stainless autoclave. The reactor was heated in an oven at 180 ^oC for 12 h before cooling to room temperature. The final white powders, which were obtained by centrifugation, were washed with deionized water and anhydrous ethanol for three times, and dried at 60 ^oC for 24 h. The TiO_2-GN nanocomposites were prepared via a surfactant-free hydrothermal reduction and assembly route (Fig. 1a). The graphene oxide (GO) sheets (Fig. S3) were synthesized by a modified Hummers method.[S1] The as-prepared TiO_2 microspheres (0.12 g) were mixed with the GO suspension (100 ml, 1.2 $mg \cdot ml^{-1}$, pH = 3-4) under vigorous stirring for 60 minutes and then were ultrasonicated for 60 minutes. 20 ml of the obtained homogeneous suspension was sealed in a 30 ml Teflon-lined stainless autoclave and placed in an oven at 180 ^oC for 12 h, generating the self-assembled TiO_2-GN hierarchical composites (Fig. 1a). The impregnation of sulfur was performed by heating TiO_2-GN nanocomposites with sulfur in a 1:(2-10) weight ratio at 200 ^oC for 12 h in a sealed vacuum tube, as illustrated in Fig. 1b and Fig. S1. The sample of sulfur confined within the TiO_2-GN hierarchical composites was referred to "S-TiO_2-GN". For comparison, reference samples of GN with S_8 (S-GN) and TiO_2 with S_8 (S-TiO_2) under the same preconditions were prepared.

Section 1.2 Material characterization

The structures of the samples were characterized using Powder X-ray diffraction (XRD), which was performed by Rigaku-Smart Lab Advance. Cu-Kα radiation (λ = 1.54Å) was used as the X-ray source, operating at 40 kV and 100 mA. A scan-speed of 0.8 sec/step and a step increment of 0.02°

over 2θ = 10°-60° were selected. The morphologies and microstructures of the samples were characterized by field emission scanning electron microscopy (FE-SEM, HITACHI S-4800) equipped with energy dispersive X-ray spectroscopy (EDS). High resolution transmission electron microscopy (HRTEM, JEOL JEM-2100) coupled with selected area electron diffraction (SAED) was used to investigate the crystallinity and microstructure of the samples. Thermal gravimetric analysis (TGA) was conducted on a TG-DSC instrument (NETZSCH STA) under O_2 with a heating rate of 10 $^oC \cdot min^{-1}$ from room temperature to 800 ^oC. Fourier Transform infrared (FT-IR) spectra were collected using a Nicolet IS10 FT-IR spectrophotometer, and the Raman spectra were collected using a Raman spectrometer (Horiba Labram HR 800, 514 nm He-Cd laser for excitation). The laser power on the sample surface was 20 mW. Surface areas of the samples were determined with N_2 adsorption at 77 K. A Coulter (Ominisorb 100cx, USA) was employed to obtain adsorption/desorption isotherms. In-situ X-ray photoelectron spectroscopy (XPS) measurements were carried out on a Thermo Scientific Nexsa XPS system with a monochromatic Al Kα radiation (hv = 1486.7 eV) and a concentric hemispherical analyzer. Before all in-situ XPS measurements, the batteries were disassembled inside an argon-filled glovebox, and the sample electrodes were carefully rinsed with 3 mL mixed solvents of 1,3-dioxolane (DOL) and 1,2-dimethoxyethane (DME) with a volume ratio of 1:1. The samples were transferred with a specially-built airtight bottle from the glovebox to the spectrometer, to avoid air exposure during the entire sample preparation and transfer processes. Core peaks were analyzed using a nonlinear Shirley-type background, and peak positions and areas were obtained by a weighted least-squares fitting of model curves (70% Gaussian and 30% Lorentzian combination). All XPS data analysis were carried out using Avantage software.

Section S1.3 Electrochemical characterization

The electrochemical measurements were carried out using CR2032-type coin cell. The cells were assembled in an argon-filled glove box (H_2O and O_2< 1 ppm). The working electrodes were prepared by pasting slurry of the S-TiO_2-GN sample and poly-(vinylidenedifluoride) (PVDF) in a weight ratio of

9:1 onto a piece of carbon cloth, and dried at 55 °C for 12 h in a vacuum. A high pure lithium foil and Celgard 2325 membrane were used as the counter electrode and the separator, respectively. The electrodes were protected by carbon paper.[S2]

The high purity electrolyte was composed of 1 M bis(trifluoromethane) sulfonamide lithium salt (LiTFSI) and 0.5 M $LiNO_3$ dissolved in mixed solvents of 1,3-dioxolane (DOL) and 1,2-dimethoxyethane (DME) with a volume ratio of 1:1. The 40-50 μl electrolytes were added in per cell. For one electrode, the active sulfur mass loading was approximately 1.8-3.2 mg/cm^2 and the area was 2 cm^2. The thickness of electrodes were approximately 50-110 μm (Fig. S7b-c). The galvanostatic discharge-charge experiments were performed over a voltage range of 1.5-2.8 V (vs. Li/Li$^+$) at different rates using a NEWARE BTS and LAND (CT2001A) battery tester. The capacities and C-rate currents were based on active materials-sulfur (1 C corresponding to 1600 mA·g^{-1}). Electrochemical impedance spectroscopy (EIS) measurements were carried out on a Gamry potentiostat by applying a sine wave with the amplitude of 10.0 mV over the frequency range from 100 kHz to 10 mHz, and the equivalent circuit by Nova software agreed well with the experimental impedance data. Cyclic voltammetry (CV) was performed using the CHI660E potentiostat at a scanning rate of 0.1 mV·s^{-1}. All cells were aged and then activated for several cycles before the cyclic test.

Section S1.4 Computational methods

First-principles calculations with the Projector Augmented Wave (PAW) method were performed by the periodic plane-wave code VASP with Generalized Gradient Approximation (GGA) functional of Perdew, Burke and Ernzerhof (PBE).[S3-S5] PAW potentials "Ti-pv", "O", "Li-sv" and "S" with 10 (including 3*p* electrons), 6, 3 and 6 valence electrons were used for Ti, O, Li and S, respectively. The energy cut off for plane wave basis was set to 450 eV. The monopole, dipole and quadrupole corrections had applied to the electrostatic interaction between the slab and its periodic images in the direction perpendicular to the slab. The atomic positions and cell parameters were relaxed until the forces on each atom are less than 0.01 eV/Å, and the self-consistent convergence accuracy was set at 1

x 10^{-5} eV.

Section S2. Results of FT-IR spectra

The FT-IR spectrum of the TiO_2-GO nanocomposites (Fig. S4b) showed distinct peaks at 3328, 1629, 1196, and 1039 cm^{-1}, indicating the existence of hydroxyl, carboxyl, and epoxy functional groups. In contrast, the same peaks were not observed on the spectra of both the TiO_2-GN nanocomposites (Fig. S4a) and the TiO_2 microspheres (Fig. S4c), indicating the reduction of GO to GN.[S6]

Section S3. Results of Raman spectra

Fig. S5a showed the Raman spectra of TiO_2-GN and TiO_2-GO nanocomposites. The D peak in Fig. S5a (at ~ 1318 cm^{-1}) was ascribed to edge planes and disordered structures associated with the disruption of symmetrical hexagonal graphitic lattice. The graphitic G peak (at ~ 1551 cm^{-1}) was ascribed to the first-order scattering of the in-plane stretching mode (E_{2g}) for symmetric sp^2 C-C bonds. An increase in the I_D/I_G ratio from 0.83 (TiO_2-GO) to 1.03 (TiO_2-GN) was observed, implying a substantial decrease of oxygen-functional groups and an increase of edge planes and disordered carbon structure in the TiO_2-GN sample.[S6] The *ex-situ* XPS survey spectra (Fig. S5b) demonstrated that the major components in both TiO_2-GN and TiO_2-GO nanocomposites were Ti ($2p_{3/2}$, 458.4 eV and $2p_{1/2}$, 464.0 eV), O (1s, 530.0 eV) and C (1s, 284.7 eV). Fig. S5c-d showed C1s XPS spectra of the TiO_2-GO and TiO_2-GN nanocomposites, respectively. The C1s peak of the TiO_2-GN nanocomposites (Fig. S5d) could be curve-fitted and assigned to C-C and C-O bonds, while that of the TiO_2-GO nanocomposites were fitted to three types of carbon bonds, i.e.C-C, C-O and C=O (Fig. S4c).[S6]

Section S4. Results of BET surface

The nanoporous structure and specific surface area of the TiO_2 microspheres and the TiO_2-GN nanocomposites were studied by nitrogen adsorption-desorption isotherms. As shown in Fig. S6a, both isotherms showed hysteresis loops of type IV for porous materials.[S7] The BET surface area of the TiO_2-

GN composites (82 $m^2 \cdot g^{-1}$) was larger than that of the TiO_2 microspheres (18 $m^2 \cdot g^{-1}$). In Fig. S6a, a remarkable adsorption at low relative pressure suggested the presence of micropores (diameter < 2 nm) within the TiO_2-GN nanocomposites, which was likely caused by the stacked GN sheets. Both samples showed adsorptions at middle pressure of p/p^o = 0.4 - 0.8 for pores and at high pressure of p/p^o = 0.9 - 1.0 for inter-particle space. The hysteresis loop of the TiO_2-GN composites was much larger than that of the TiO_2 microspheres, suggesting that the spaces between GN sheets and the TiO_2 microspheres provided large surface area and porosity. The pore size distributions were calculated using the Barrett-Joyner-Halenda (BJH) model.[S7] Such three-dimensional TiO_2/GN framework (the Fig. 2d-f) is beneficial for (1) diffusion of nanosized sulfur into the nanocomposites, (2) efficient intercalation/deintercalation of Li^+ ions, and (3) high-speed electron transfer through the GN network.

Section S5. Results of TGA

The large surface area of the TiO_2-GN nanocomposites allowed to load high amount of sulfur. As determined by TGA analysis (Fig. S7), the mass ratio of TiO_2-GN : S_8 was 0.38:0.62 in the S-TiO_2-GN composites, and the mass ratio of TiO_2 : GN was 0.97:0.03 in the TiO_2-GN composites.

References

S1. Q. Su, S. Pang, V. Alijani, C. Li, X. Feng and K. Müllen, Composites of graphene with large aromatic molecules, *Adv Mater.*, 2009, **21**, 3191-3195.

S2. Y. Zhao, Q. Sun, X. Li, C. Wang, Y. Sun, K. Adair, R. Li and X. Sun, Carbon paper interlayers: A universal and effective approach for highly stable Li metal anodes, *Nano Energy*, 2018, **43**, 368-375.

S3. P. Blochl, Projector augmented-wave method, *Phys. Rev. B*, 1994, **50**, 17953-17979.

S4. G. Kresse, J. Furthmüller, Efficient iterative schemes for ab initio total-energy calculations using a plane-wave basis set, *Phys. Rev. B*, 1996, **54**, 11169-11186.

S5. J. Perdew, K. Burke and M. Ernzerhof, Generalized Gradient Approximation Made Simple, *Phys.*

Rev. Lett., 1996, **77**, 3865-3868.

S6. D. Chen, H. Feng, J. Li, Graphene oxide: preparation, functionalization, and electrochemical applications, *Chem. Rev.*, 2012, **112**, 6027-6053.

S7. J. Villarroel-Rocha, D. Barrera, K. Sapag, Introducing a self-consistent test and the corresponding modification in the Barrett, Joyner and Halenda method for pore-size determination, *Microporous Mesoporous Mater.*, 2014, **200**, 68-78.

Table S1. Electrochemical performance of the S-TiO_2-GN nanocomposite (this work) and other similar cathode materials reported in literatures.

Electrodes (sulfur loading, wt %)	Testing conditions (the current density at cycling times)	Sulfur mass Loading (mg/cm^2)	Final Capacity ($mAh\ g^{-1}$)	References
S-TiO_2-GN (62%)	2.6 mA/cm^2 at 200 times	3.2	700	This work
S-TiO_2-GN (62%)	2.6 mA/cm^2 at 200 times	2.3	870	This work
S-TiO_2-GN (62%)	2.6 mA/cm^2 at 600 times	1.8	583	This work
TiO@C-HS/S (70%)	0.67 mA/cm^2 at 500 times	1.5	750	[S1]
TiO@C-HS/S (70%)	0.33 mA/cm^2 at 50 times	4	821	[S1]
S-TiO_2 (45%)	0.28 mA/cm^2 at 200 times	0.86	890	[S2]
S-TiO_2 (71%)	0.42 mA/cm^2at 1000 times	0.4-0.6	690	[S3]
PCNTs-S@G/3%T (82%)	0.86 mA/cm^2 at 250 times	1.2	600	[S4]
PCNTs-S@G (51%)	0.86 mA/cm^2 at 300 times	0.51	1040	[S4]
S-Ti_4O_7 (60-70%)	0.13 mA/cm^2 at 250 times	0.75-0.9	800	[S5]
S-Ti_4O_7 (64%)	0.02 C at 100 times	NA	1034	[S6]
S-3DTiO_2 (51%)	0.5-0.6 mA/cm^2 at 240 times	1.5-2.0	797	[S7]
S-3DTiO_2 (51%)	2.5-3.3 mA/cm^2 at 700 times	1.5-2.0	608	[S7]
S-GN-ALDTiO_2 (73%)	2.1-3.0 mA/cm^2 at 1000 times	1.3-1.8	918	[S8]
C-TiO_2-C (76.4%)	2 C at 500 times	2.5	511	[S9]
GC-TiO@CHF (75%)	0.2 C at 400 times	5.0	680	[S10]
GTS (55%)	1C at 400 times	1.5-2	732	[S11]

References

S1. Z. Li, J. Zhang, B. Guan, D. Wang, L. Liu and X. Lou, A sulfur host based on titanium monoxide@carbon hollow spheres for advanced lithium-sulfur batteries, *Nat. Commun.*, 2016, **7** 13065.

S2. Z. Liang, G. Zheng, W. Li, Z. Seh, H. Yao, K. Yan, D. Kong and Y. Cui, Sulfur cathodes with hydrogen reduced titanium dioxide inverse opal structure, *ACS Nano*, 2014, **8**, 5249-5256.

S3. Z. Seh, W. Li, J. Cha, G. Zheng, Y. Yang, M. McDowell, P. Hsu and Y. Cui, Sulphur-TiO_2 yolk-shell nanoarchitecture with internal void space for long-cycle lithium-sulphur batteries, *Nat. Commun.*, 2013, **4**, 1331.

S4. Z. Xiao, Z. Yang, L. Wang, H. Nie, M. Zhong, Q. Lai , X. Xu, L. Zhang and S. Huang, A light weight TiO_2/graphene interlayer, applied as a highly effective polysulfide absorbent for fast, long-life lithium-sulfur batteries, *Adv. Mater.*, 2015, **27**, 2891-2898.

S5. Q. Pang, D. Kundu, M. Cuisinier and L. Nazar, Surface-enhanced redox chemistry of polysulphides on a metallic and polar host for lithium-sulphur batteries, *Nat. Commun.*, 2014, **5**, 4759.

S6. X. Tao, J. Wang, Z. Ying, Q. Cai, G. Zheng, Y. Gan, H. Huang, Y. Xia, C. Liang, W. Zhang and Y.

Cui, Strong sulfur binding with conducting magnéli-Phase Ti_nO_{2n-1} nanomaterials for improving lithium-sulfur batteries, *Nano Lett.*, 2014, **14**, 5288-5294.

S7. T. Lei, Y. Xie, X. Wang, S. Miao, J. Xiong and C. Yan, TiO_2 feather duster as effective polysulfides restrictor for enhanced electrochemical kinetics in lithium-sulfur batteries, *Small*, 2017, **13**, 1701013.

S8. M. Yu, J. Ma, H. Song, A. Wang, F. Tian, Y. Wang, H. Qiu and R.Wang, Atomic layer deposited TiO_2 on a nitrogen-doped graphene/sulfur electrode for high performance lithium-sulfur batteries, *Energy Environ. Sci.*, 2016, **9**, 1495-1503.

S9. M. Fang, Z. Chen, Y. Liu, J. Quan, C. Yang, L. Zhu, Q. Xu and Q. Xu, Design and synthesis of novel sandwich-type C@TiO_2@C hollow microspheres as efficient sulfur hosts for advanced lithium-sulfur batteries, *J. Mater. Chem. A*, 2018, **6**, 1630-1638.

S10. Z. Li, B. Guan, J. Zhang and X. Lou, A compact nanoconfined sulfur cathode for high-performance lithium-sulfur batteries, *Joule*, 2017, **1**, 576-587.

S11. L. Gao, M. Cao, Y. Fu Z. Zhong, Y. Shen and M. Wang, Hierarchical TiO_2 spheres assisted with graphene for a high performance lithium-sulfur battery, *J. Mater. Chem. A*, 2016, **4**, 16454-16461.

Table S2. Equivalent circuit parameters calculated from the EIS analysis.

Parameter	Cycle	S-TiO_2-GN
R_S / ohm	Befor cycle	1.66 ohm
	100th	8.87 ohm
	200th	8.35 ohm
R_p / ohm	Befor cycle	53.4 ohm
	100th	3.14 ohm
	200th	3.70 ohm

Fig. S1 The optical image of sulfur loading in a vacuum tube device.

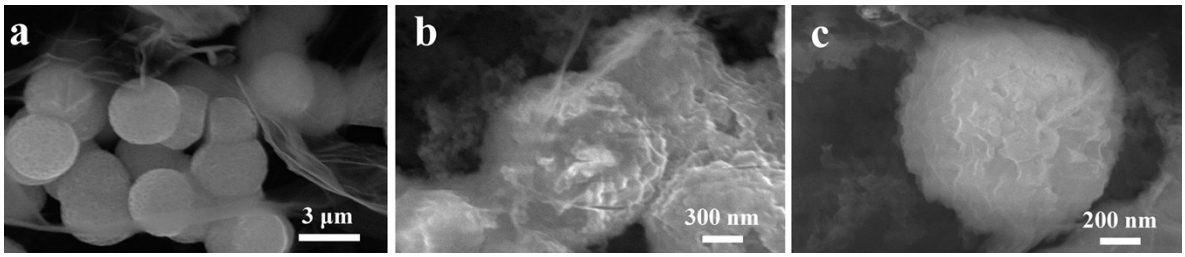

Fig. S2 The FE-SEM images of S-TiO_2-GN nanocomposites.

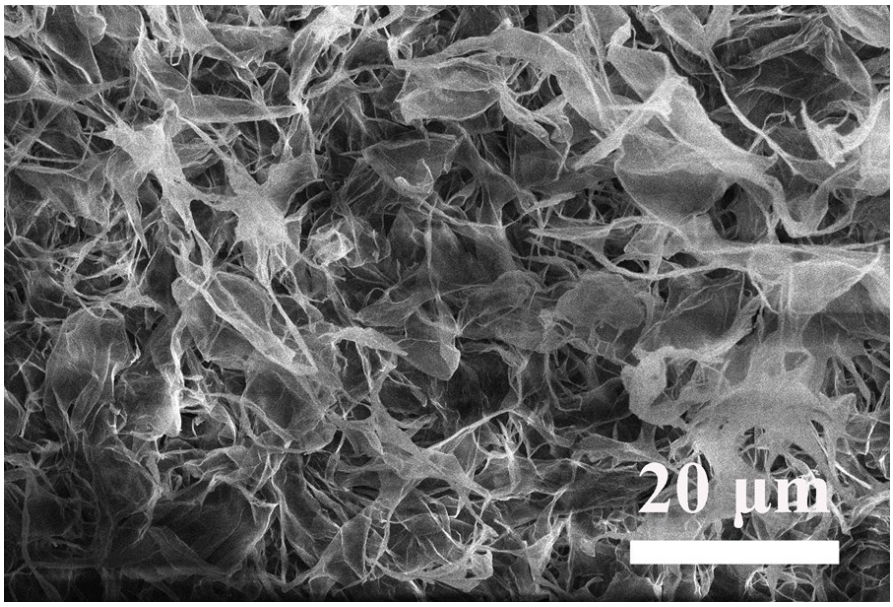

Fig. S3 The FE-SEM image of the as-synthesized GO sheets.

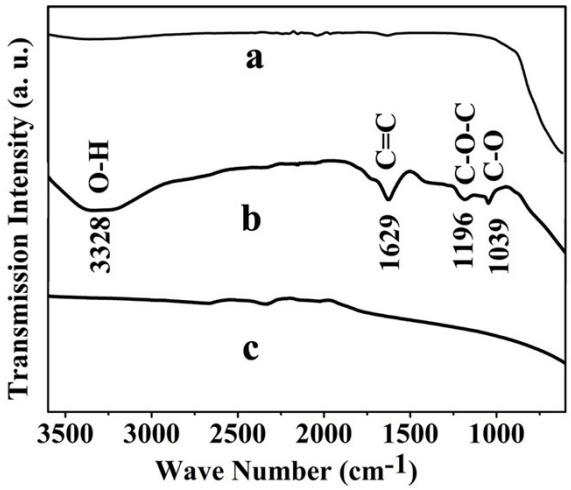

Fig. S4 FT-IR spectra of (a) TiO_2-GN nanocomposites, (b) TiO_2-GO nanocomposites, and (c) TiO_2 microspheres.

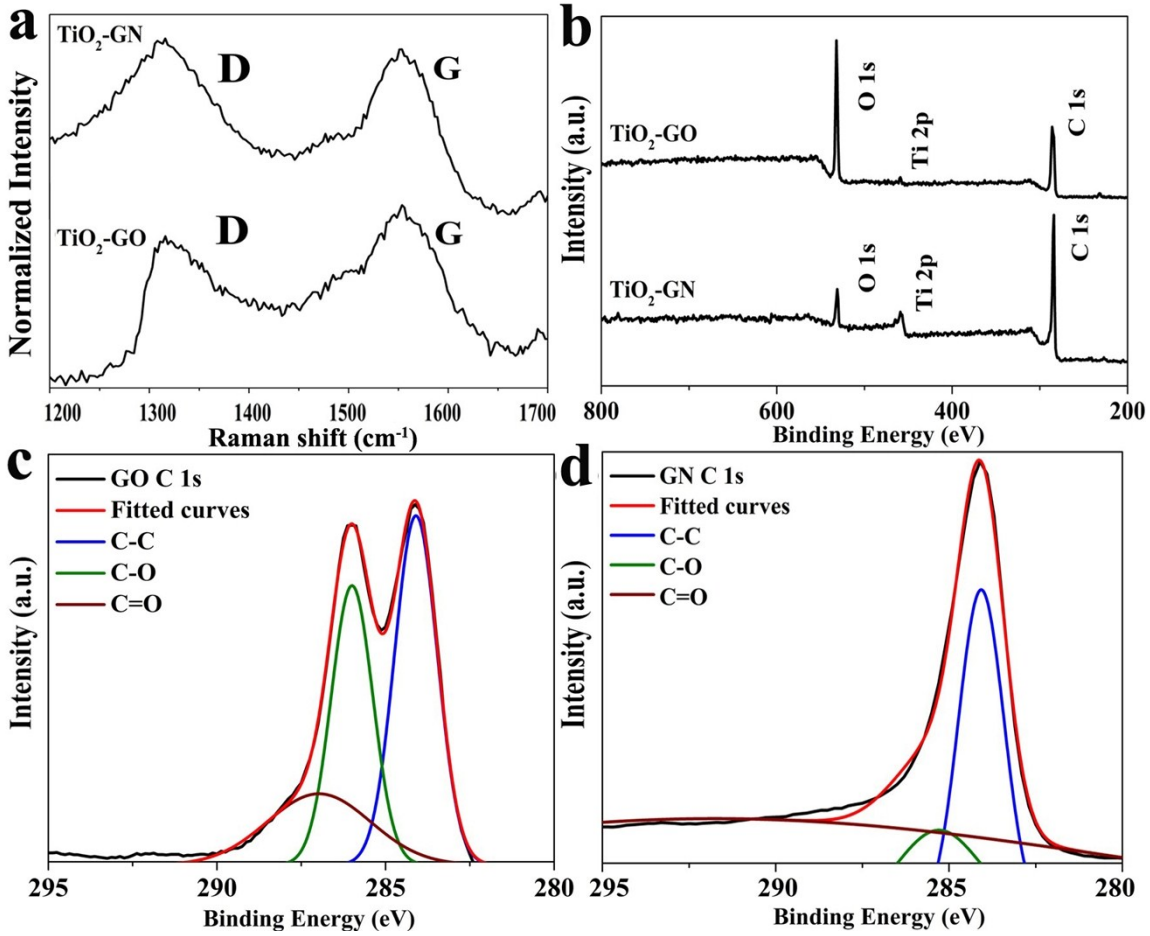

Fig. S5 (a) Raman spectra of TiO_2-GO and TiO_2-GN nanocomposites, (b) *ex-situ* XPS survey spectra of TiO_2-GO and TiO_2-GN nanocomposites, and C_{1s} spectra of (c) TiO_2-GO nanocomposites and (d) TiO_2-GN nanocomposites.

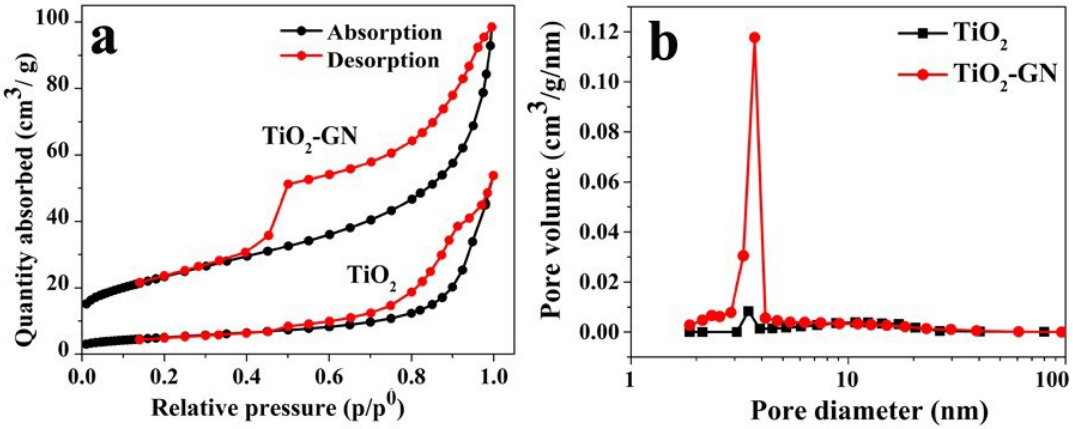

Fig.S6 (a) N_2 adsorption–desorption isotherms and (b) BJH pore size distributions of TiO_2-GN nanocomposites (TiO_2-GN) and the reference TiO_2 microspheres (TiO_2).

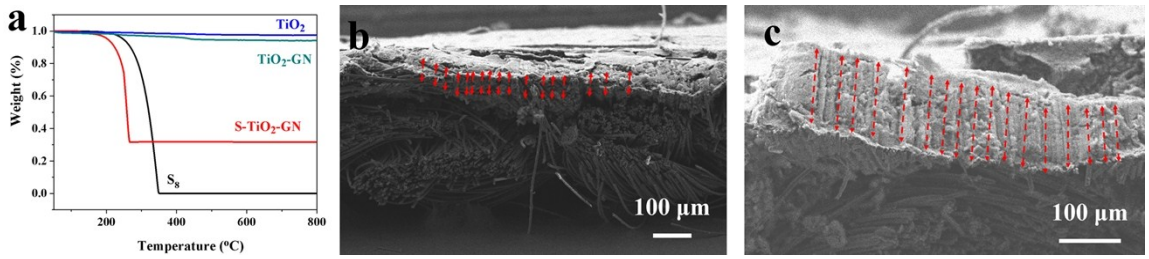

Fig. S7 TGA curves (a) of S_8, TiO_2 microspheres (TiO_2), TiO_2-GN nanocomposites (TiO_2-GN), and S-TiO_2-GN nanocomposites (S-TiO_2-GN). The cross-view FESEM images of the S-TiO_2-GN with 1.8 and 3.2 mg/cm^2 sulfur mass loading (b-c), and red line mark thickness area.

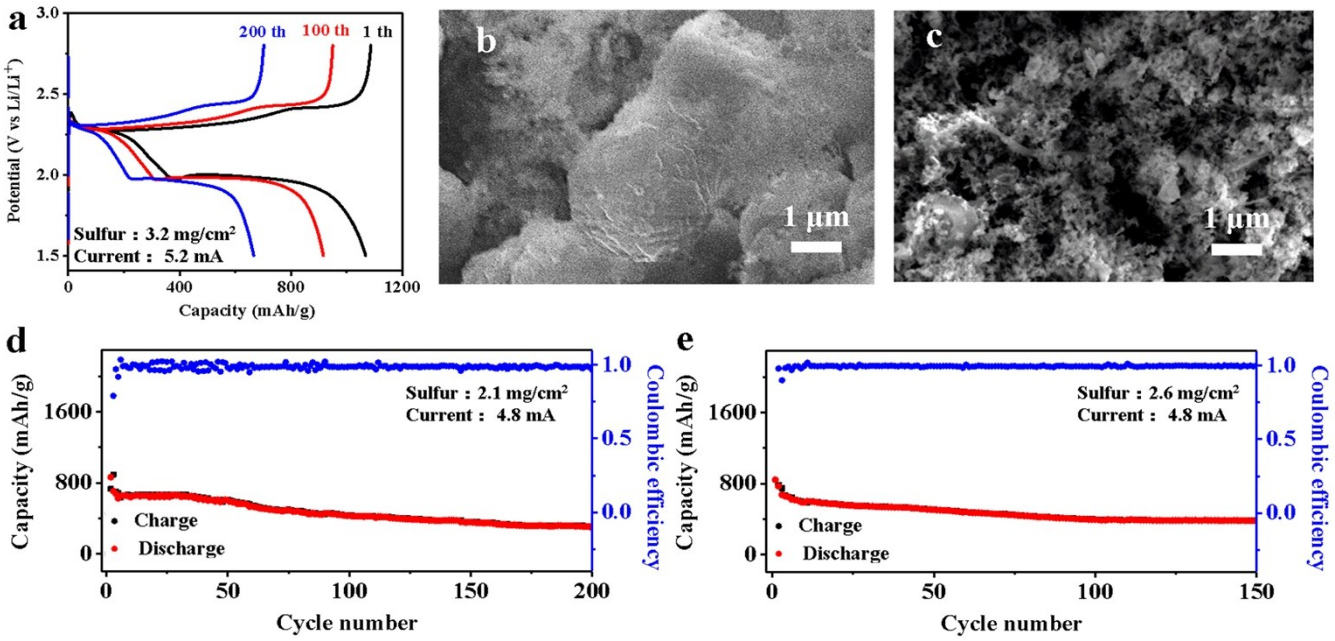

Fig. S8 Galvanostatic charge and discharge profiles of S-TiO_2-GN with 3.2 mg/cm^2 sulfur loading under 5.2 mA (a). FE-SEM images of S-TiO_2 (b) and S-GN (c) cathodes, and Galvanostatic charge/discharge behavior and Coulombic efficiency of the cells prepared using S-TiO_2 (d) and S-GN (e) cathodes.

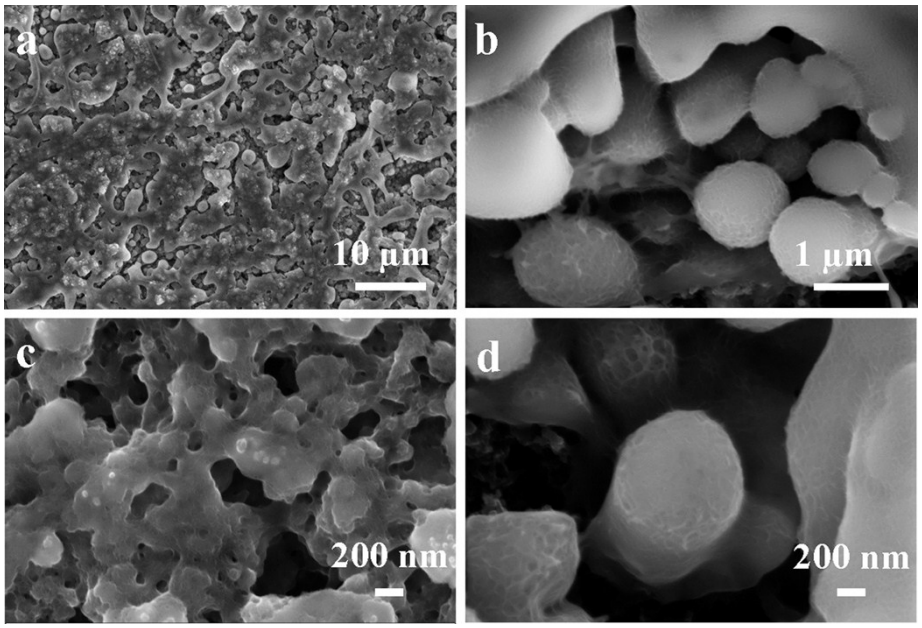

Fig. S9 FE-SEM images of S-TiO_2-GN electrodes after cell running.

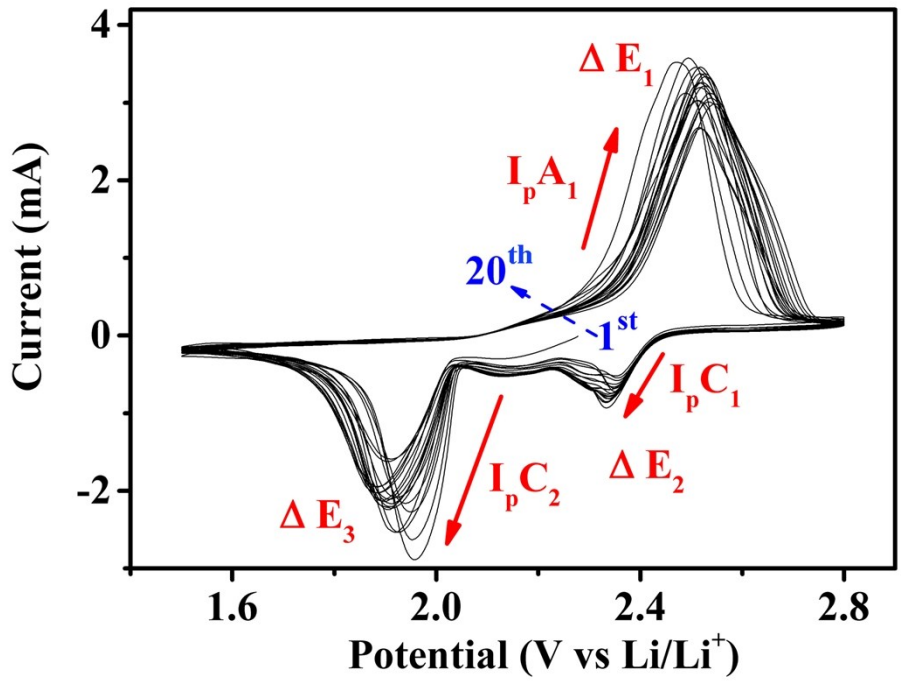

Fig. S10 Cyclic-voltammograms of S-GN electrodes scanned from 1st to 20th with the scan rate of 0.1 mV/s

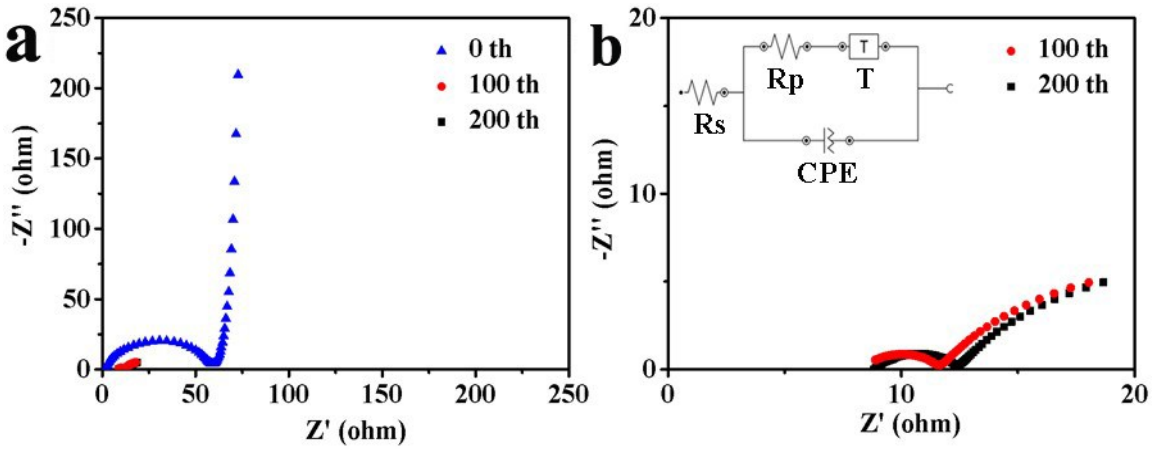

Fig. S11 Nyquist plots (a-b) of the cell with S-TiO_2-GN electrodes before cycling (0^{th}), at 100^{th} and 200^{th} cycles at 5.2 mA. Inset: the equivalent circuit of the S-TiO_2-GN electrodes.

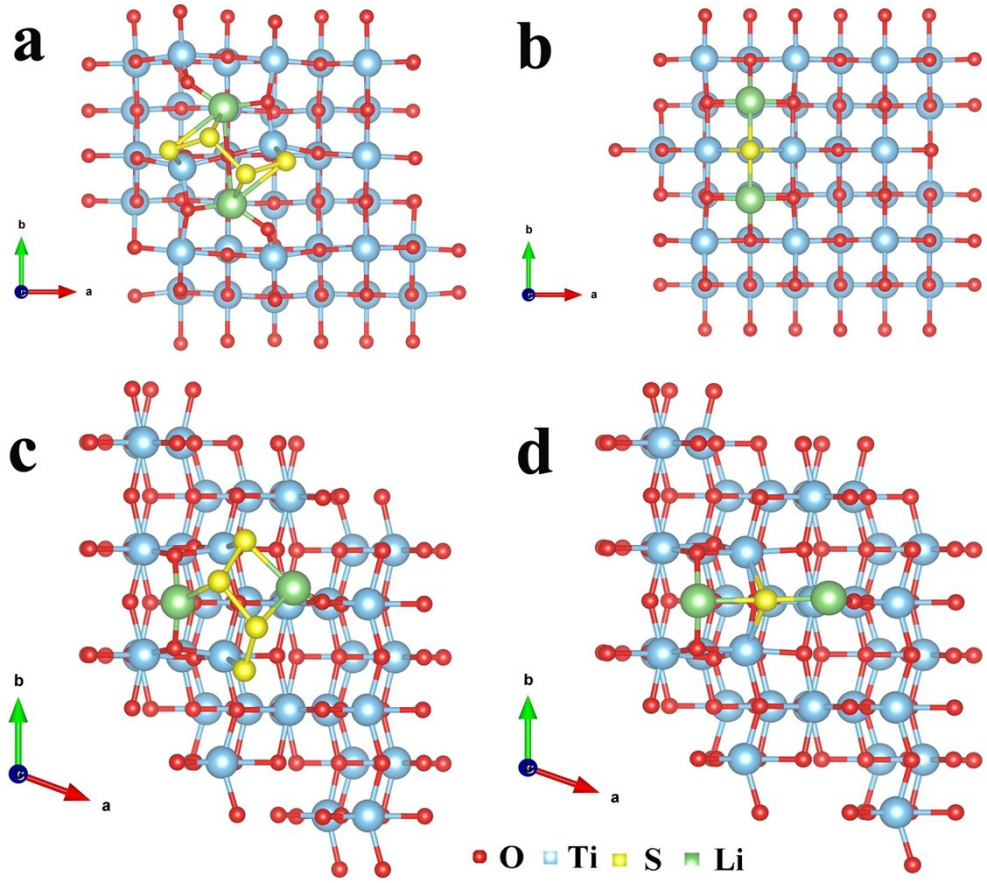

Fig. S12 Top views of the optimized stable configurations of the adsorption of Li_2S_4 (a and c) and Li_2S (b and d) molecules on (001) (a, b) and (101) (c, d) facets of an anatase TiO_2.